ACS APPLIED MATERIALS & INTERFACES

www.acsami.org

Research Article

Micromolecule Postdeposition Process for Highly Efficient Inverted Perovskite Solar Cells

Bing'e Li, Jiangping Xing, Valeriya Budnik, Chuangping Liu, Qinghua Cao, Fobao Xie, Xiaoli Zhang,* Hui Liu,* Andrei Stsiapanau,* and Xiao Wei Sun

Cite This: *ACS Appl. Mater. Interfaces* 2025, 17, 14269−14277

Read Online

ACCESS | Metrics & More | Article Recommendations | Supporting Information

ABSTRACT: Inverted perovskite solar cells (PSCs) have achieved great development, contributed by the advance of self-assembled monolayer (SAM) hole-transporting layers (HTLs) due to their distinctive molecular designability. However, SAM HTLs still present challenges of achieving a compact and ordered surface, resulting in vacancies and defects at the interface as well as adversely affecting the growth of perovskites. In this work, we propose a micromolecule postdeposition process to design the SAM HTL interface and form high-quality perovskites to achieve highly efficient inverted PSCs. We introduce etidronic acid (EA) as a postdeposition micromolecule to fill and reduce vacancies at the SAM interface and to improve growing high-quality perovskites. The postdeposition EA can anchor to the substrate through P−OH anchors, occupying vacancies left by MeO-4PACz, and simultaneously create interaction with perovskites by P═O and C−OH functional groups. The micromolecule postdeposition process effectively fills and reduces vacancies at the SAM interface, passivates defects of perovskites, and facilitates carrier transport. Consequently, a champion PCE of 24.42% is achieved for the target PSCs, which is much higher than the efficiency (20.08%) of the control. This research provides a guided and widely applicable strategy for the development of the SAM interface and further advances the performance of PSCs.

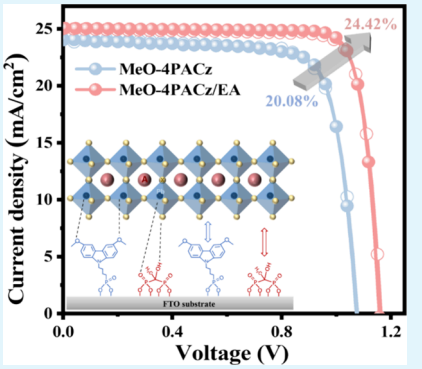

KEYWORDS: *micromolecule postdeposition process, reducing vacancies at the interface, hole transport layer, facilitating the growth of perovskites, perovskites solar cells*

INTRODUCTION

Perovskite solar cells (PSCs) have achieved significant advancements over the past decade, reaching an impressive power conversion efficiency (PCE) of over 26%.[1−3] Inverted p-i-n PSCs are regarded as one of the promising routes for commercialization application due to the rapid improvement of efficiency, stability, and compatibility with the tandem devices.[4−6] The large efficiency enhancement of inverted PSCs is a result of the development of self-assembled monolayer (SAM) hole-transporting layers (HTLs) and passivation strategies. SAM molecules comprise terminal groups that determine functionalities and interaction with the perovskite upper layer, a linker by employment of alkyl chains and aromatic groups, and anchor groups that act with metal oxides and chemically attach to the substrate surface.[7−9] Typically, popular anchor groups include the carboxylic acid group and phosphonic acid group, which present diverse types of absorption and different binding energies with substrates.[10,11] Moreover, the intermolecular dipole moment and the deviation angle between SAM molecules and the perovskite layer can be adjusted by introduction of diverse groups or atoms (e.g., O, N, and Br), contributing to restraining defects at bottom interfaces of perovskite layers, reinforcing interaction with perovskites, and facilitating carrier extraction by modifying energy levels.[12−14] Therefore, SAM molecules show attractive advantages of distinctive molecular designability as well as low-cost and simple fabrication processes and present great opportunities for cost-effective, scalable, and stable HTLs in inverted PSCs.[15]

However, the commonly employed SAM molecules in PSCs, such as 2PACz, 4PACz, Me-4PACz, MeO-2PACz, and MeO-4PACz, still present some shortcomings.[16,17] To be more specific, ensuring compact and ordered interfaces of SAM molecules for the desired growth of perovskite films, as well as evaluating uniformity and defects, are still challenging. Moreover, these ultrathin organic SAM layers are easy to be decomposed under UV light and thermal conditions, which present disadvantages for the long-term stability of PSCs.[18] Many new SAM molecules have been developed by leveraging their self-assembly advantages. Chen et al. designed a carbazole-based SAM (Ph-4PACz) as the HTL by modifying

Received: December 23, 2024
Revised: February 5, 2025
Accepted: February 11, 2025
Published: February 24, 2025

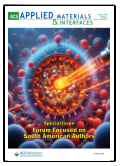

https://doi.org/10.1021/acsami.4c22563
ACS Appl. Mater. Interfaces 2025, 17, 14269−14277

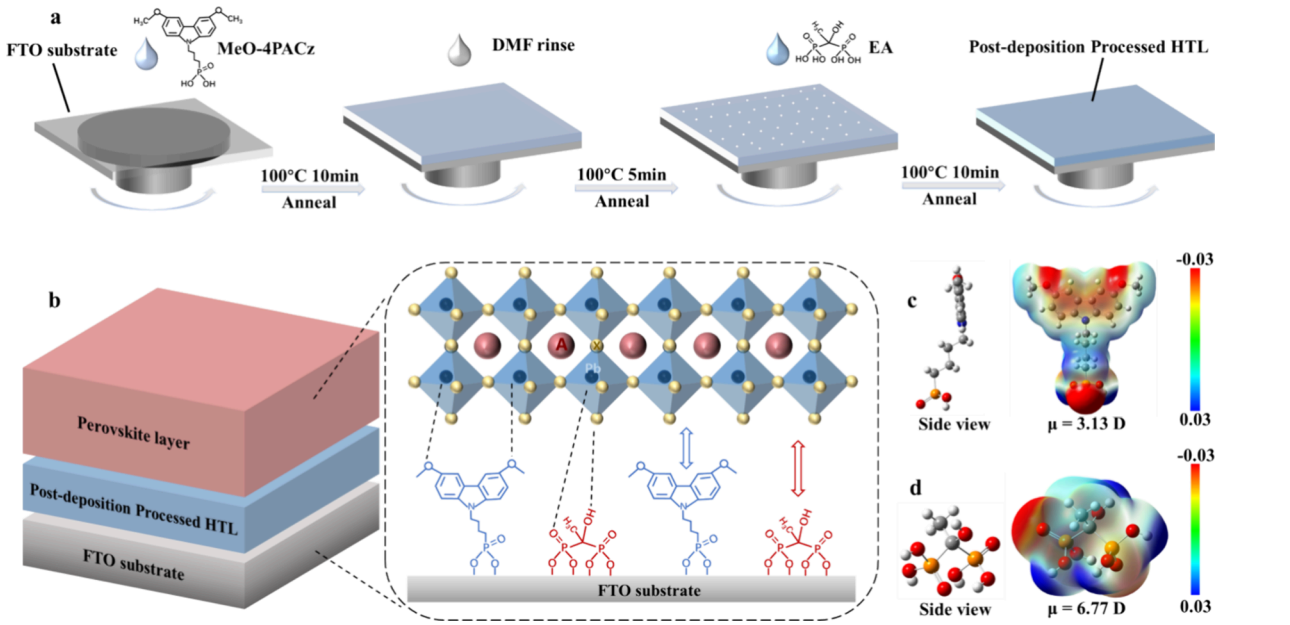

Figure 1. (a) Diagram of the micromolecule postdeposition process for forming hte MeO-4PACz/EA HTL interface. (b) Illustration of interactions by the EA postdeposition process. Electrostatic potential (φ) distributions of (c) MeO-4PACz and (d) EA obtained using Gaussian calculations.

the carbazole group of Me-4PACz and symmetrically linking a benzene ring to the carbazole group, which aims to improve charge transfer and energy-level alignment through increasing the dipole moment.[19] Furthermore, Zhu et al. proposed another carbazole-based SAM (MeO-4PADBC) acting with nickel oxide (NiO_x) nanoparticles to form a hole-selective NiO_x/MeO-4PADBC layer, significantly improving the interaction and stability of the interface between NiO_x and perovskites.[20] Nevertheless, approaches to designing new SAM molecules are costly and still cannot totally avoid the formation of defects and vacancies at the interface due to the incomplete coverage and weak interaction with the substrate. Typically, a dimethylformamide (DMF) rinsing process is employed to remove the weak physical adsorption of hydrogen bond, to reduce the accumulation of molecules in the substrate, and to facilitate the deposition of a subsequent layer. However, it possibly diminishes the coverage rate and leads to vacancies of SAM molecules at the interface, adversely affecting the growth of perovskites.[21−23] The vacancies at the interface between SAM and perovskite layers resulted in severe nonradiative recombination and hindered carrier transport, leading to the largely decreased performance of PSCs.[24,25] Therefore, it is highly crucial to develop new strategies that are low-cost and facile and that can effectively reduce vacancies and defects at the interface, as well as facilitate the growth of high-quality perovskite films.

Herein, we propose a micromolecule postdeposition process to design the SAM HTL interface and form high-quality perovskites to achieve efficient and stable inverted PSCs. We select 4-(3,6-dimethoxycarbazol-9-yl) ethyl phosphonic acid (MeO-4PACz) as the primary SAM HTL and apply etidronic acid (EA) as a postdeposition micromolecule to fill and reduce vacancies at the SAM interface and simultaneously to improve growing high-quality perovskite films. Without affecting the transmittance of MeO-4PACz layer, the postdeposition EA can anchor to the substrate through P−OH anchors, occupying vacancies left by MeO-4PACz, and simultaneously can create interaction with perovskites by P═O and C−OH functional groups. As a result, this postdeposition process effectively fills and reduces vacancies at the SAM HTL interface, passivates defects of perovskites, as well as facilitates carrier transport. Finally, by employing the EA postdeposition strategy, a champion efficiency of 24.42% is achieved for the target PSCs, which is much higher than the efficiency (20.08%) of the control device. This research provides a guided and widely applicable strategy for the development of the SAM interface and further advances the performance of PSCs.

RESULTS AND DISCUSSION

The EA micromolecule postdeposition process is illustrated in Figure 1a. Two commercially available molecules of MeO-4PACz and EA (molecular structures are shown in Figure S1, Supporting Information) are used for the deposition of the HTL layer. Initially, MeO-4PACz is utilized to deposit the primary HTL layer on the fluorine-doped tin oxide (FTO) substrate. Then, a typical step of DMF rinsing is performed to eliminate unstable anchored hydrogen bonds and excessive accumulation of primary SAM for better formation of perovskite film but would inevitably create some vacancies. The vacancies can be inferred from the phenomenon of the contact potential difference (CPD) of film surfaces (Figure S2, Supporting Information). After DMF rinsing, the film shows some extent of increase of CPD, which suggests that DMF rinsing removes weakly anchored SAM molecules and thus possibly leads to the exposure of FTO substrate and vacancies. Finally, the EA micromolecule postdeposition process is introduced to fill and reduce vacancies at the SAM interface, facilitating the growth of high-quality perovskite film. The HTL substrate of MeO-4PACz with EA postdeposition shows a reduced contact angle for the perovskite precursor solution depositing on the substrate (Figure S3, Supporting Information), evidencing the improved wettability and coverage for perovskite film formation. The designed HTL interface with robust functional interactions is illustrated in Figure 1b, and

https://doi.org/10.1021/acsami.4c22563
ACS Appl. Mater. Interfaces 2025, 17, 14269−14277

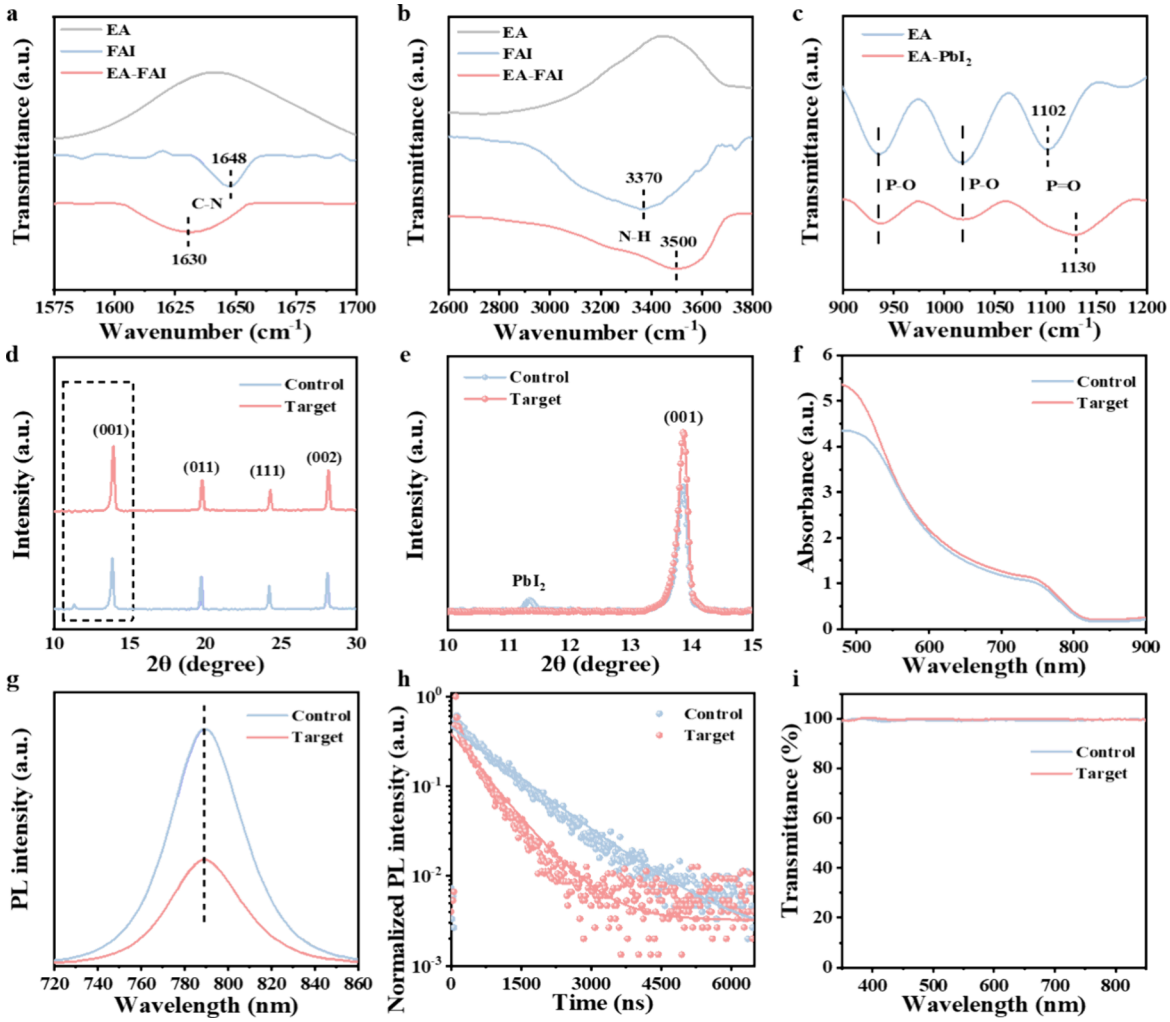

Figure 2. FTIR spectra of (a, b) EA interacting with FAI and (c) EA interacting with PbI_2, (d) XRD spectra from 10 to 30°, and (e) partial spectra from 10 to 15° of perovskite films. (f) Absorbance spectra of perovskites. (g) PL and (h) TRPL of perovskites tested with a structure of FTO/HTL/perovskites. (i) Transmittance spectra of HTLs (control: FTO/MeO-4PACz; target: FTO/MeO-4PACz/EA).

the electrostatic potential (φ) distributions of MeO-4PACz and EA, derived from Gaussian calculations, are depicted in Figure 1c,d, respectively. It is inferred that the C−OH and P═O groups of EA can interact with FAI and PbI_2 of perovskites, thereby passivating defects at the bottom interface of perovskites.[26] Meanwhile, the four P−OH groups can anchor onto the FTO substrate through dehydration condensation to form a bisphosphonic acid anchoring structure,[27−29] which effectively fills vacancies at the SAM interface and ultimately reduces defects, facilitating the charge carrier transport and decreasing nonradiative recombination.

We initially statistically investigate and determine an ideal concentration of postdeposition EA micromolecule for HTL of PSCs. As shown in Figure S4 and Table S1 in the Supporting Information, the device performance is gradually enhanced with the increase of EA, and the best performance is achieved when the concentration of postdeposition EA reaches an optimal value of 0.5 mg/mL. The improvement originates from the functional interactions, reduced steric hindrance of smaller alkyl chains, and vacancy reduction by the introduction of the EA micromolecule.[30−33] Further excess EA would lead to detrimental molecular aggregation, which adversely decreases the device efficiency. In the later discussion, the perovskite film or the device prepared on MeO-4PACz/EA (optimal concentration of 0.5 mg/mL) is regarded as the target group, and those formed on bare MeO-4PACz HTL without the employment of postdeposition EA are termed as the control.

To verify chemical interactions by the introduction of postdeposition EA micromolecules, Fourier transform infrared spectroscopy (FTIR) characterization is conducted. As presented in Figure 2a,b, the introduction of EA induces peak shifts of FAI. The C−N peak shifts from 1648 to 1630 cm^{-1}, while the N−H peak moves from 3370 to 3500 cm^{-1}, which indicates the hydrogen-bond interaction between the N atoms of FAI and −OH groups of EA. Furthermore, it is also observed that the P═O peak of EA shifts from 1102 to 1130 cm^{-1} after mixing with PbI_2, while no change occurs for P−O peaks. This suggests that P═O groups of EA can coordinate with Pb^{2+} ions to help reduce residual PbI_2 in perovskites, whereas P−OH groups participate in the dehydration condensation reaction with the FTO substrate, without engaging directly in the interaction with PbI_2.[26] Full ranges of FTIR spectra are shown in Figure S5, Supporting Information. The above results confirm that postdeposition EA molecules contribute to interacting with perovskites and the substrate simultaneously to robust the interface and effectively alleviate defects.

https://doi.org/10.1021/acsami.4c22563
ACS Appl. Mater. Interfaces 2025, 17, 14269−14277

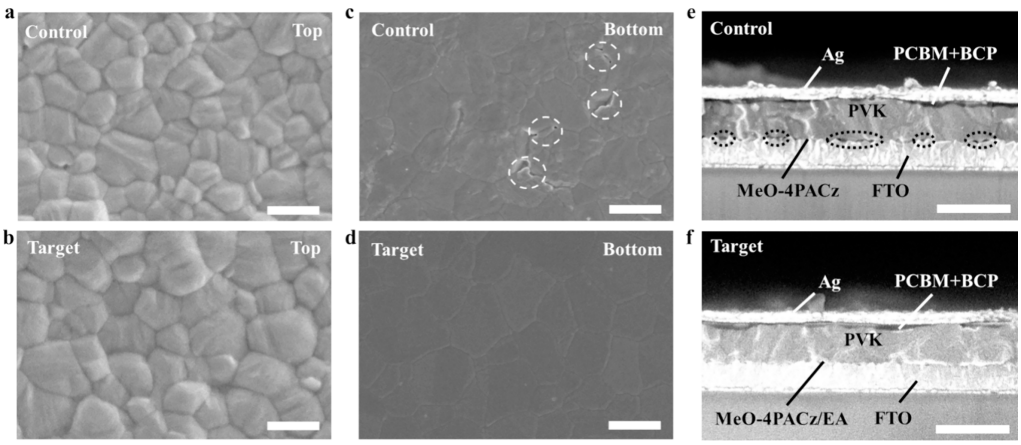

Figure 3. SEM images of the top surface of (a) control and (b) target perovskite films and SEM images of the bottom surface of (c) control and (d) target perovskite films. The scale bar is 500 nm. Cross-sectional SEM images of (e) control and (f) target perovskite films. The scale bar is 1000 nm.

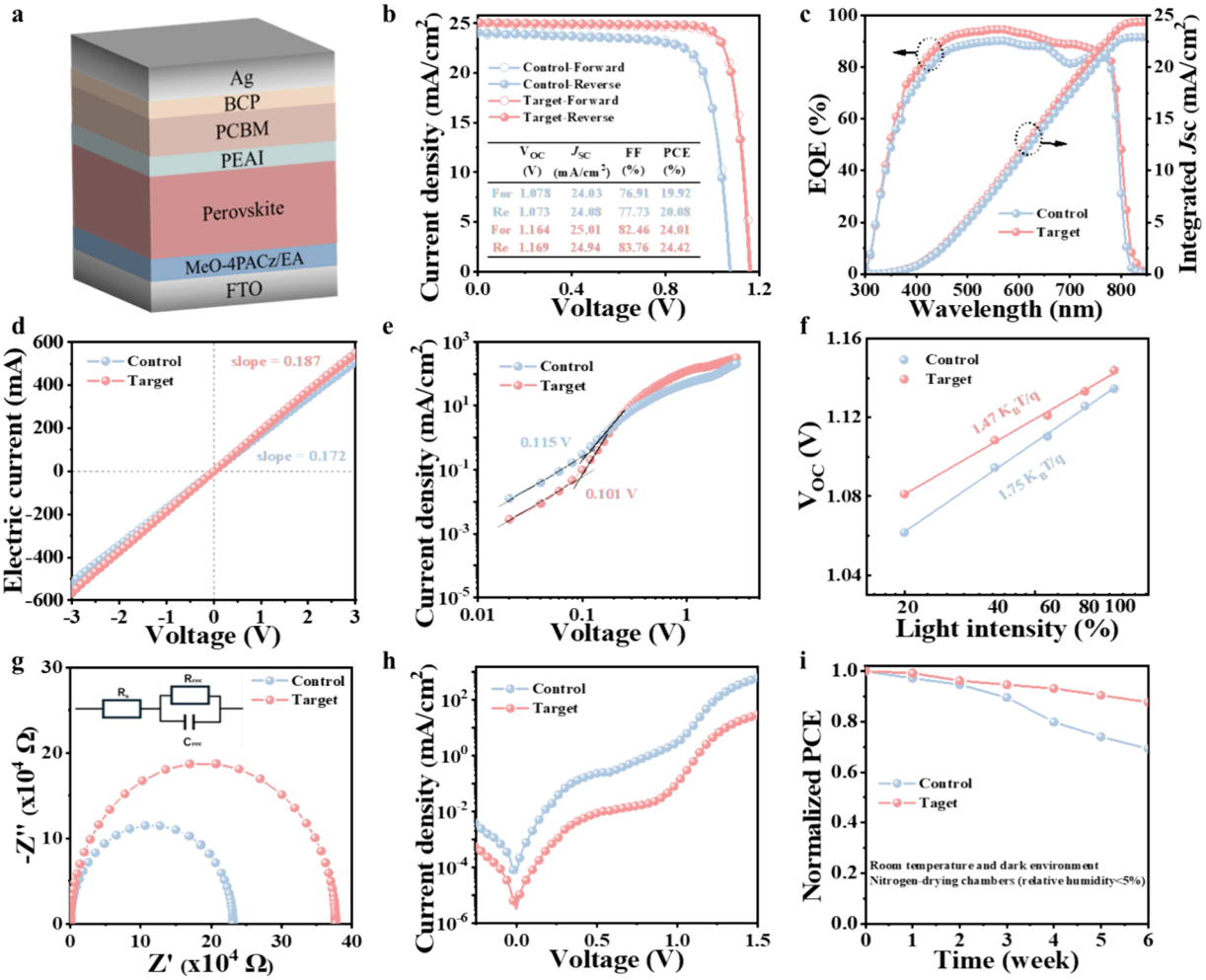

Figure 4. (a) Device structure diagram of inverted PSCs. (b) Forward and reverse scanning performance of control and champion target PSCs. (c) EQE of control and champion target PSCs. (d) Conductivities of HTLs. Characterization structures are FTO/MeO-4PACz/Ag for the control and FTO/MeO-4PACz/EA/Ag) for the target. (e) SCLC of devices. Characterization structures are FTO/MeO-4PACz/perovskite/Spiro/Ag for the control and FTO/MeO-4PACz/EA/perovskite/Spiro/Ag for the target. (f) Light intensity dependence of the V_{OC} of PSCs. (g) EIS of PSCs. (h) Dark $J-V$ curves of PSCs. (i) Storage stability of PSCs stored at room temperature and a nitrogen-filled environment with a relative humidity of <5%.

We then explore influences of the employment of the micromolecule postdeposition process on the crystallization of perovskites and charge carrier dynamics between the HTL and perovskite film by conducting X-ray diffraction (XRD), ultraviolet−visible spectroscopy (UV−vis), steady-state photoluminescence (PL), and time-resolved photoluminescence

https://doi.org/10.1021/acsami.4c22563
ACS Appl. Mater. Interfaces 2025, 17, 14269−14277

(TRPL) measurements. As shown in Figure 2d,e, crystallinities of perovskite peaks are obviously enhanced after employment of the EA postdeposition process on the SAM HTL. Especially, the diffraction intensity of the (001) lattice plane of perovskite shows significant enhancement, while the peak of PbI_2 around 11.2° is diminished. This result verifies the FTIR result that the interaction between P═O groups of EA and Pb^{2+} of perovskites leads to the decrease of residual PbI_2 and helps passivate defects at the bottom of perovskites.[26,34] Moreover, the improved light absorption intensity of the perovskite film also indicates the enhanced crystallization quality by the employment of EA (Figure 2f). Band gaps of perovskite films do not show obvious changes (Figure S6, Supporting Information). In addition, the target perovskite film deposited on MeO-4PACz/EA shows a lower PL intensity than the control film (Figure 2g), indicating the facilitated and accelerated charge carrier extraction.[35] Meanwhile, the lifetime of the target perovskite film is also shortened due to the efficient charge transport (Figure 2h).[36,37] By fitting the lifetime curves following the equation $I(t) = I_0 + A_1\exp(-t/\tau_1) + A_2\exp(-t/\tau_2)$, where τ_1 and τ_2 represent the fast and slow decay time, the lifetimes of perovskite films formed on bare MeO-4PACz and MeO-4PACz/EA are obtained to be 926.08 to 485.84 ns, respectively (Table S2, Supporting Information). Moreover, we employ Kelvin probe force microscopy (KPFM) to explore the effect of postdeposition EA on the surface electronic chemical potential of perovskites. The target perovskite film presents a lower surface contact potential difference (Figure S7, Supporting Information), which is conducive to the Fermi-level downward shift of the film and is beneficial for the hole extraction.[38] This observation is in accordance with the facilitated charge carrier transport obtained in PL and TRPL results. It is noted that the employment of the EA micromolecule postdeposition process does not affect the transmittance (Figure 2i) of the HTL layer, which shows almost zero absorbance (Figure S8, Supporting Information). In conclusion, the designed MeO-4PACz/EA HTL interface effectively contributes to passivating defects, accelerating charge carrier extraction and transport as well as increasing the crystal crystallinity of perovskites.

Impacts of the postdeposition EA micromolecule on the top and bottom morphologies of perovskite films are investigated by scanning electron microscopy (SEM) and cross-sectional SEM. As illustrated in Figure 3a,b, the top surface of the target perovskite film shows a relatively larger grain size (~262 nm) than the control (~246 nm) as well as a denser and smoother morphology, suggesting that the designed MeO-4PACz/EA by employing postdeposition EA facilitates the growth of high-quality perovskite grains. The distribution histogram of perovskite grain sizes is presented in Figure S9, Supporting Information. Moreover, atomic force microscopy (AFM) is applied to investigate the surface roughness of perovskite films (Figure S10, Supporting Information). The employment of postinserting EA decreases the surface roughness of perovskites from 20.5 (control) to 19.3 nm (target), implying that the growth of perovskite grains becomes more uniform and smoother. Meanwhile, we utilized ultraviolet (UV) glue to obtain the bottom surfaces of perovskite films to observe bottom morphologies. As shown in Figure 3c,d, the bottom surface of the control film exhibits obvious cracks and holes around grain boundaries. In contrast, the target perovskite film presents a smooth and dense bottom interface, which is contributed by the functional interactions at the bottom interface and would enhance the contact and adhesion between the HTL and perovskite layer.[39,40] Furthermore, cross-sectional SEM reveals that the employment of post-deposition EA effectively reduces and repairs vacancies at the bottom surface (Figure 3e,f), helping to minimize defects at the interface of HTL and perovskites. In a brief conclusion, the above results demonstrate that the EA micromolecule postdeposition process greatly aids in improving the growth of perovskite grains, enhancing the interaction between HTL and the perovskite layer, as well as effectively reducing vacancies and defects.

We fabricate the control and target PSCs based on a device structure of FTO/HTL/perovskite/PEAI/PCBM/BCP/Ag (Figure 4a) and conduct forward and reverse scans for both devices (as depicted in Figure 4b). The champion PCE of target PSCs reaches a value of 24.42% in the reverse scan, which is much higher than that of the control device (20.08%). In the forward scan, the PCE increases from 19.92 (control) to 24.01% (target). The great increase of efficiency mainly originates from the substantial enhance of the fill factor (FF) (improving from 76.91 to 82.46% in the forward scan and raising from 77.73 to 83.76% in reverse scan), along with the large improvement of the open-circuit voltage (*Voc*) as well as the short-circuit current density (J_{sc}). Additionally, external quantum efficiency (EQE) values of control and target devices are shown in Figure 4c. The target PSCs achieve an integrated current density of 24.4 mA/cm^2, which is close to the J_{sc} obtained.

The significant enhancement of device efficiency mainly stems from introducing the EA micromolecule postdeposition process filling and reducing vacancies at the HTL interface, as well as passivating defects of perovskites. We investigate the conductivity of HTLs of PSCs by utilizing the following formula for conductivity:

$$\sigma = \frac{I}{V} \times \frac{d}{A} \tag{1}$$

where I represents the current, V denotes the voltage, d is the sample length, and A signifies the sample area. Given that both the volume and dimensions of samples are consistent, the increased conductivity correlates with the enhanced I/V ratio.[41] As illustrated in Figure 4d, the I/V ratio increases from 0.172 of the control sample to 0.187 of the target sample, suggesting that the employment of postdeposition EA effectively enhances the electrical conductivity of HTL. The enhancement of conductivity is associated with the reduction of the trap density of HTL by the employment of postdeposition EA.[30] We conduct space charge limited current (SCLC) measurements to characterize hole trap density within devices. The trap filling limiting voltage (V_{TFL}) can be defined by the intersection point between the ohmic region and the trap-filling region, as shown in Figure 4e.[42] The hole trap-state density can be calculated using the following equation:

$$V_{TFL} = \frac{en_tL^2}{2\varepsilon_r\varepsilon_0} \tag{2}$$

where e represents the elementary charge, ε_r denotes the relative dielectric constant of perovskites, ε_0 is the vacuum permittivity, L signifies the thickness of perovskite film, and n_t indicates the trap-state density.[43] A V_{TFL} value of 0.115 V is derived for the control and 0.101 V for the target sample, respectively. Consequently, the hole trap density is observed to

https://doi.org/10.1021/acsami.4c22563
ACS Appl. Mater. Interfaces 2025, 17, 14269−14277

be decreasing from 5.65×10^{14} cm^{-3} for the control to a lower value of 4.96×10^{14} cm^{-3} for the target, further confirming that the introduction of the EA micromolecule postdeposition process can effectively contribute to reducing vacancies and defects. Furthermore, we examine recombination characteristics within PSCs through the analysis of ideality factors. The light-intensity-dependent V_{OC} can be expressed by the following equation:

$$qV_{OC} = E_g + mK_BT\ln(I) \quad (3)$$

where q is the elementary charge, E_g denotes the band gap energy, m refers to the ideality factor, K_B stands for Boltzmann's constant, T symbolizes the absolute temperature, and I indicates the light intensity. The ideality factor approaching 1 suggests reduced nonradiative recombination and thus enhanced device performance.[44] As shown in Figure 4f, the ideality factor of PSCs decreases from 1.75 (control) to 1.47 (target), which implies that the vacancies and defects are effectively passivated by the employment of postdeposition EA, leading to largely suppressed nonradiative recombination.

Electrochemical impedance spectroscopy (EIS) is conducted to quantitatively explore the recombination resistance (R_{re}) and series resistance (R_s) of PSCs.[45,46]Figure 4g presents the Nyquist plots with an equivalent circuit of devices. The R_{re} of devices increases from 231170 Ω of the control device to 376730 Ω of target PSCs, while the R_s decreases from 20.42 (control) to 16.95 Ω (target). This result suggests that the designed MeO-4PACz/EA with the employment of postdeposition EA effectively facilitates charge transport and reduces carrier recombination rate within the device. Moreover, as shown in Figure 4h, the dark current of target PSCs is significantly decreased, further confirming the reduced vacancies and defects within the device based on the designed MeO-4PACz/EA by the micromolecule postdeposition process.[47,48] Finally, we assess long-term stabilities of PSCs stored at room temperature and a nitrogen-filled environment with a relative humidity of <5%. As depicted in Figure 4i, the target PSCs show a distinctly slower degradation of efficiency after storing for 6 weeks. It retains approximately 87% of the initial PCE, while the control device only maintains 69% of the efficiency. Consequently, with the introduction of the EA micromolecule postdeposition process, PSCs show significantly prolonged storing stability.

CONCLUSIONS

In summary, we propose a micromolecule postdeposition process to design the SAM HTL interface and form high-quality perovskites to achieve efficient and stable inverted PSCs. MeO-4PACz is selected as the primary SAM HTL, and EA is employed as the postdeposition micromolecule to fill and reduce vacancies at the SAM interface and simultaneously to improve growing high-quality perovskite films. The post-inserted EA can anchor to the substrate through P−OH anchors, occupying vacancies left by MeO-4PACz, and can create interaction with perovskites by P═O and C−OH functional groups. Consequently, the micromolecule postdeposition process effectively fills and reduces vacancies at the SAM HTL interface, passivates defects of perovskites, as well as facilitates carrier transport. Finally, a champion PCE of 24.42% is achieved for the target PSCs by employing the micromolecule postdeposition process, which is much higher than the efficiency (20.08%) of the control device. This research provides a guided and widely applicable strategy for the development of the SAM interface and further advances the performance of PSCs.

EXPERIMENTAL SECTION

Materials. Methylammonium bromide (MABr, 99.99%), leaching iodide (PbI_2, 99.99%), and bromocresol purple (BCP, 99.99%) were purchased from Advanced Election Technology Co., Ltd. Methylammonium chloride (MACl, 99.99%), cesium iodide (CsI, 99.99%), lead bromide ($PbBr_2$, 99.99%), formamidine hydroiodide (FAI, 99.99%), and [6,6]-phenyl C61 butyric acid methyl ester ($PC_{61}BM$, 99.99%) were purchased from Xi'an Yuri Solar Co., Ltd. Methylammonium iodide (MAI, 99.99%) and 2-phenylethylamine Hydroiodide (PEAI, 99.99%) were purchased from Xian Polymer Light Technology Corp. *n*,*n*-Dimethylformamide (DMF, 99.99%), dimethyl sulfoxide (DMSO, 99.99%), chlorobenzene (CB, 99.99%), ethanol, and etidronic acid (EA, 99.99%) were purchased from Sigma-Aldrich. 4-(3,6-Dimethoxycarbazol-9-yl) ethyl phosphonic acid (MeO-4PACz, 99.99%) was purchased from Derthon Optoelectronics Materials Science Technology Co., Ltd.

Device Fabrication. First, FTO substrates were cleaned with DI water, acetone, and isopropanol in an ultrasound bath for 20 min followed by UV ozone treatment for 30 min. Cleaned substrates were transferred to the glovebox for solution deposition. Second, MeO-4PACz (1 mg/mL dissolved in ethanol) was deposited on the FTO substrate at 3000 rpm for 30 s followed by annealing at 100 °C for 10 min. After DMF was dynamically washed at 4000 rpm for 30 s, it was annealed again at 100 °C for 5 min. Thereafter, different concentrations of EA were dissolved in ethanol and spin-coated onto the MeO-4PACz substrate at 3000 rpm for 30 s followed by annealing at 100 °C for 10 min. Third, a perovskite precursor solution was prepared with 6.7 mg MABr, 8.8 mg MACl, 18.2 mg CsI, 196.1 mg FAI, 22 mg $PbBr_2$, and 572 mg PbI_2 in 865 μL DMF and DMSO solution (volume ratio 4:1) and stirred for 6 h. The perovskite precursor solution was spin-coated at 1000 rpm for 5 s and then at 4000 rpm for 30 s onto the HTL. When 15 s remained on the countdown, CB antisolvent was dropped onto the substrates followed by annealing at 100 °C for 50 min. Afterward, PEAI and MAI (in a mass ratio of 2:1) dissolved in the IPA and DMF solution (with a volume ratio of 150:1) were dynamically spin-coated at 5000 rpm for 30 s followed by annealing at 100 °C for 5 min. Fourthly, the PCBM (20 mg/mL dissolved in CB) was spin-coated at 1500 rpm for 30 s followed by annealing at 100 °C for 10 min. Subsequently, BCP (0.5 mg/mL dissolved in IPA) was dynamically spin-coated at 4000 rpm for 30 s. Finally, Ag (100 nm) was thermally evaporated as an electrode.

Characterizations. Current density−voltage (J−V) curves of PSCs were measured with a Keithley 2400 digital source meter under a simulated solar source of AM1.5 G (100 mW/cm^2, Wacom Denso Co., Japan). The PSC device was equipped with a shading mask with an aperture area of 0.04 cm^2 to ensure the accuracy of the current density in J−V curves. The FTIR spectrum was recorded with a reflectance (ATR) instrument (PerkinElmer Spectrum 100, USA) from 300 to 4000 cm^{-1}. The surface morphology of perovskite films was characterized by scanning electron microscopy (SEM, JEOL JSM-7800F Prime, Japan). The XRD patterns for perovskite film crystallization analysis were measured by X-ray diffraction (XRD) using a Bruker D2 Phaser with Cu Kα radiation. The steady-state photoluminescence spectrum (PL) and time-resolved photoluminescence spectrum (TRPL) were measured with a fluorescence spectrophotometer (FLS980, Edinburgh Instruments). UV−vis spectra were measured on a UV−vis spectrometer (UV-3600). EQE was measured by an EnLi Technology (Taiwan) EQE measurement system. The EIS and SCLC tests were measured by an electrochemical workstation (Donghua DH7000C). The surface roughness and potential were tested using a MultiMode 8 and Dimension Icon Atomic Force Microscope (AFM, Bruker) with a tapping amplitude modulation mode.

https://doi.org/10.1021/acsami.4c22563
ACS Appl. Mater. Interfaces 2025, 17, 14269−14277

■ ASSOCIATED CONTENT

Supporting Information

The Supporting Information is available free of charge at https://pubs.acs.org/doi/10.1021/acsami.4c22563.

Molecular structures, CPD results, contact angles, device performance comparation, whole FTIR spectra, TOC plots of the absorbance spectra, KPFM, absorbance spectra, particle dimension distribution histogram, AFM, average device performance data, and TRPL fitting data (PDF)

■ AUTHOR INFORMATION

Corresponding Authors

Xiaoli Zhang − *School of Physics and Optoelectronic Engineering, Guangdong Provincial Key Laboratory of Sensing Physics and System Integration Applications, Guangdong University of Technology, Guangzhou 510006, China;* orcid.org/0000-0002-3603-0653; Email: xlzhang@tju.edu.cn

Hui Liu − *School of Physics and Optoelectronic Engineering, Guangdong Provincial Key Laboratory of Sensing Physics and System Integration Applications, Guangdong University of Technology, Guangzhou 510006, China;* orcid.org/0009-0000-7798-1247; Email: liuhui@gdut.edu.cn

Andrei Stsiapanau − *Department of Micro- and Nanoelectronics, Belarusian State University of Informatics and Radioelectronics (BSUIR), Minsk 220013, Republic of Belarus*; Email: stepanov@bsuir.by

Authors

Bing'e Li − *School of Physics and Optoelectronic Engineering, Guangdong Provincial Key Laboratory of Sensing Physics and System Integration Applications, Guangdong University of Technology, Guangzhou 510006, China*

Jiangping Xing − *School of Physics and Optoelectronic Engineering, Guangdong Provincial Key Laboratory of Sensing Physics and System Integration Applications, Guangdong University of Technology, Guangzhou 510006, China*

Valeriya Budnik − *Department of Micro- and Nanoelectronics, Belarusian State University of Informatics and Radioelectronics (BSUIR), Minsk 220013, Republic of Belarus*

Chuangping Liu − *School of Physics and Optoelectronic Engineering, Guangdong Provincial Key Laboratory of Sensing Physics and System Integration Applications, Guangdong University of Technology, Guangzhou 510006, China*

Qinghua Cao − *School of Physics and Optoelectronic Engineering, Guangdong Provincial Key Laboratory of Sensing Physics and System Integration Applications, Guangdong University of Technology, Guangzhou 510006, China*

Fobao Xie − *School of Physics and Optoelectronic Engineering, Guangdong Provincial Key Laboratory of Sensing Physics and System Integration Applications, Guangdong University of Technology, Guangzhou 510006, China*

Xiao Wei Sun − *Department of Electronic and Electrical Engineering, Southern University of Science and Technology, Shenzhen 518055, China;* orcid.org/0000-0002-2840-1880

Complete contact information is available at: https://pubs.acs.org/10.1021/acsami.4c22563

Notes

The authors declare no competing financial interest.

■ ACKNOWLEDGMENTS

This research was supported by the Natural Science Foundation of Guangdong Province (2023A1515011467) and was financially supported by the Guangdong University of Technology SPOE Seed Foundation (SF2024111507).

■ REFERENCES

(1) Yang, Y.; Chen, H.; Liu, C.; Xu, J.; Huang, C.; Malliakas, C. D.; Wan, H.; Bati, A. S. R.; Wang, Z.; Reynolds, R. P.; Gilley, I. W.; Kitade, S.; Wiggins, T. E.; Zeiske, S.; Suragtkhuu, S.; Batmunkh, M.; Chen, L. X.; Chen, B.; Kanatzidis, M. G.; Sargent, E. H. Amidination of Ligands for Chemical and Field-Effect Passivation Stabilizes Perovskite Solar Cells. *Science* **2024**, *386* (6724), 898−902.

(2) Green, M. A.; Dunlop, E. D.; Yoshita, M.; Kopidakis, N.; Bothe, K.; Siefer, G.; Hinken, D.; Rauer, M.; Hohl-Ebinger, J.; Hao, X. Solar Cell Efficiency Tables (Version 64). *Progress in Photovoltaics: Research and Applications* **2024**, *32* (7), 425−441.

(3) Gong, C.; Li, H.; Xu, Z.; Li, Y.; Wang, H.; Zhuang, Q.; Wang, A.; Li, Z.; Guo, Z.; Zhang, C.; Wang, B.; Li, X.; Zang, Z. Efficient and Stable Inverted Perovskite Solar Cells Enabled by Homogenized PCBM with Enhanced Electron Transport. *Nat. Commun.* **2024**, *15* (1), 9154.

(4) Zhang, H.; Park, N.-G. Progress and Issues in p-i-n Type Perovskite Solar Cells. *DeCarbon* **2024**, *3*, No. 100025.

(5) Hu, L.; Li, M.; Yang, K.; Xiong, Z.; Yang, B.; Wang, M.; Tang, X.; Zang, Z.; Liu, X.; Li, B.; Xiao, Z.; Lu, S.; Gong, H.; Ouyang, J.; Sun, K. PEDOT:PSS Monolayers to Enhance the Hole Extraction and Stability of Perovskite Solar Cells. *Journal of Materials Chemistry A* **2018**, *6* (34), 16583−16589.

(6) Sun, K.; Chang, J.; Isikgor, F. H.; Li, P.; Ouyang, J. Efficiency Enhancement of Planar Perovskite Solar Cells by Adding Zwitterion/LiF Double Interlayers for Electron Collection. *Nanoscale* **2015**, *7* (3), 896−900.

(7) Ullah, A.; Park, K. H.; Lee, Y.; Park, S.; Faheem, A. B.; Nguyen, H. D.; Siddique, Y.; Lee, K.-K.; Jo, Y.; Han, C.-H.; Ahn, S.; Jeong, I.; Cho, S.; Kim, B.; Park, Y. S.; Hong, S. Versatile Hole Selective Molecules Containing a Series of Heteroatoms as Self-Assembled Monolayers for Efficient p-i-n Perovskite and Organic Solar Cells. *Adv. Funct. Mater.* **2022**, *32* (49), No. 2208793.

(8) Zhou, Y.; Huang, X.; Zhang, J.; Zhang, L.; Wu, H.; Zhou, Y.; Wang, Y.; Wang, Y.; Fu, W.; Chen, H. Interfacial Modification of NiO*x* for Highly Efficient and Stable Inverted Perovskite Solar Cells. *Adv. Energy Mater.* **2024**, *14* (25), No. 2400616.

(9) Li, L.; Wei, M.; Carnevali, V.; Zeng, H.; Zeng, M.; Liu, R.; Lempesis, N.; Eickemeyer, F. T.; Luo, L.; Agosta, L.; Dankl, M.; Zakeeruddin, S. M.; Roethlisberger, U.; Grätzel, M.; Rong, Y.; Li, X. Buried-Interface Engineering Enables Efficient and 1960-h ISOS-L-2I Stable Inverted Perovskite Solar Cells. *Adv. Mater.* **2024**, *36* (13), No. 2303869.

(10) Zhang, Z.; Zhu, R.; Tang, Y.; Su, Z.; Hu, S.; Zhang, X.; Zhang, J.; Zhao, J.; Xue, Y.; Gao, X.; Li, G.; Pascual, J.; Abate, A.; Li, M. Anchoring Charge Selective Self-Assembled Monolayers for Tin−Lead Perovskite Solar Cells. *Adv. Mater.* **2024**, *36* (18), No. 2312264.

(11) Park, D.-A.; Zhang, C.; Park, N.-G. Strain-Less Perovskite Film Engineered by Interfacial Molecule for Stable Perovskite Solar Cells. *ACS Energy Letters* **2024**, *9* (5), 2428−2435.

(12) Al-Ashouri, A.; Köhnen, E.; Li, B.; Magomedov, A.; Hempel, H.; Caprioglio, P.; Márquez, J. A.; Morales Vilches, A. B.; Kasparavicius, E.; Smith, J. A.; Phung, N.; Menzel, D.; Grischek, M.; Kegelmann, L.; Skroblin, D.; Gollwitzer, C.; Malinauskas, T.; Jošt, M.; Matič, G.; Rech, B.; Schlatmann, R.; Topič, M.; Korte, L.; Abate, A.; Stannowski, B.; Neher, D.; Stolterfoht, M.; Unold, T.; Getautis, V.; Albrecht, S. Monolithic Perovskite/Silicon Tandem Solar Cell with >

29% Efficiency by Enhanced Hole Extraction. *Science* **2020**, *370* (6522), 1300−1309.
(13) Al-Ashouri, A.; Magomedov, A.; Roß, M.; Jošt, M.; Talaikis, M.; Chistiakova, G.; Bertram, T.; Márquez, J. A.; Köhnen, E.; Kasparavičius, E.; Levcenco, S.; Gil-Escrig, L.; Hages, C. J.; Schlatmann, R.; Rech, B.; Malinauskas, T.; Unold, T.; Kaufmann, C. A.; Korte, L.; Niaura, G.; Getautis, V.; Albrecht, S. Conformal Monolayer Contacts with Lossless Interfaces for Perovskite Single Junction and Monolithic Tandem Solar Cells. *Energy Environ. Sci.* **2019**, *12* (11), 3356−3369.
(14) Levine, I.; Al-Ashouri, A.; Musiienko, A.; Hempel, H.; Magomedov, A.; Drevilkauskaite, A.; Getautis, V.; Menzel, D.; Hinrichs, K.; Unold, T.; Albrecht, S.; Dittrich, T. Charge Transfer Rates and Electron Trapping at Buried Interfaces of Perovskite Solar Cells. *Joule* **2021**, *5* (11), 2915−2933.
(15) Zhang, S.; Ye, F.; Wang, X.; Chen, R.; Zhang, H.; Zhan, L.; Jiang, X.; Li, Y.; Ji, X.; Liu, S.; Yu, M.; Yu, F.; Zhang, Y.; Wu, R.; Liu, Z.; Ning, Z.; Neher, D.; Han, L.; Lin, Y.; Tian, H.; Chen, W.; Stolterfoht, M.; Zhang, L.; Zhu, W.-H.; Wu, Y. Minimizing Buried Interfacial Defects for Efficient Inverted Perovskite Solar Cells. *Science* **2023**, *380* (6643), 404−409.
(16) Li, M.; Liu, M.; Qi, F.; Lin, F. R.; Jen, A. K. Y. Self-Assembled Monolayers for Interfacial Engineering in Solution-Processed Thin-Film Electronic Devices: Design, Fabrication, and Applications. *Chem. Rev.* **2024**, *124* (5), 2138−2204.
(17) Zhong, L.; Liu, C.; Lai, S.; Li, B. e.; Zheng, B.; Zhang, X. Recent Advances in Self-Assembled Molecular Application in Solar Cells. *Nanomaterials* **2024**, *14* (9), 779.
(18) Magomedov, A.; Al-Ashouri, A.; Kasparavičius, E.; Strazdaite, S.; Niaura, G.; Jošt, M.; Malinauskas, T.; Albrecht, S.; Getautis, V. Self-Assembled Hole Transporting Monolayer for Highly Efficient Perovskite Solar Cells. *Adv. Energy Mater.* **2018**, *8* (32), No. 1801892.
(19) Sun, A.; Tian, C.; Zhuang, R.; Chen, C.; Zheng, Y.; Wu, X.; Tang, C.; Liu, Y.; Li, Z.; Ouyang, B.; Du, J.; Li, Z.; Cai, J.; Chen, J.; Wu, X.; Hua, Y.; Chen, C.-C. High Open-Circuit Voltage (1.197 V) in Large-Area (1 cm^2) Inverted Perovskite Solar Cell via Interface Planarization and Highly Polar Self-Assembled Monolayer. *Adv. Energy Mater.* **2024**, *14* (8), No. 2303941.
(20) Li, Z.; Sun, X.; Zheng, X.; Li, B.; Gao, D.; Zhang, S.; Wu, X.; Li, S.; Gong, J.; Luther, J. M.; Li, Z. a.; Zhu, Z. Stabilized Hole-Selective Layer for High-Performance Inverted p-i-n Perovskite Solar Cells. *Science* **2023**, *382* (6668), 284−289.
(21) Tang, H.; Shen, Z.; Shen, Y.; Yan, G.; Wang, Y.; Han, Q.; Han, L. Reinforcing Self-Assembly of Hole Transport Molecules for Stable Inverted Perovskite Solar Cells. *Science* **2024**, *383* (6688), 1236−1240.
(22) Zheng, X.; Li, Z.; Zhang, Y.; Chen, M.; Liu, T.; Xiao, C.; Gao, D.; Patel, J. B.; Kuciauskas, D.; Magomedov, A.; Scheidt, R. A.; Wang, X.; Harvey, S. P.; Dai, Z.; Zhang, C.; Morales, D.; Pruett, H.; Wieliczka, B. M.; Kirmani, A. R.; Padture, N. P.; Graham, K. R.; Yan, Y.; Nazeeruddin, M. K.; McGehee, M. D.; Zhu, Z.; Luther, J. M. Co-Deposition of Hole-Selective Contact and Absorber for Improving the Processability of Perovskite Solar Cells. *Nature Energy* **2023**, *8* (5), 462−472.
(23) Meggiolaro, D.; Motti, S. G.; Mosconi, E.; Barker, A. J.; Ball, J.; Andrea Riccardo Perini, C.; Deschler, F.; Petrozza, A.; De Angelis, F. Iodine Chemistry Determines the Defect Tolerance of Lead-Halide Perovskites. *Energy Environ. Sci.* **2018**, *11* (3), 702−713.
(24) Mao, L.; Yang, T.; Zhang, H.; Shi, J.; Hu, Y.; Zeng, P.; Li, F.; Gong, J.; Fang, X.; Sun, Y.; Liu, X.; Du, J.; Han, A.; Zhang, L.; Liu, W.; Meng, F.; Cui, X.; Liu, Z.; Liu, M. Fully Textured, Production-Line Compatible Monolithic Perovskite/Silicon Tandem Solar Cells Approaching 29% Efficiency. *Adv. Mater.* **2022**, *34* (40), No. 2206193.
(25) Zuo, L.; Gu, Z.; Ye, T.; Fu, W.; Wu, G.; Li, H.; Chen, H. Enhanced Photovoltaic Performance of $CH_3NH_3PbI_3$ Perovskite Solar Cells through Interfacial Engineering Using Self-Assembling Monolayer. *J. Am. Chem. Soc.* **2015**, *137* (7), 2674−2679.
(26) Zhang, Y.; Kong, T.; Liu, Y.; Liu, X.; Liu, W.; Saliba, M.; Bi, D. The Effect of Self-Assembled Bridging Layer on the Performance of Pure $FAPbI_3$-Based Perovskite Solar Cells. *Adv. Funct. Mater.* **2024**, *34* (30), No. 2401391.
(27) Liu, R.; Xu, J.; Hu, T.; Li, X.; Wang, K.; Huang, Q.; Duan, Z.; Liu, H.; Qian, W.; Zhou, H.; Cong, C.; Yue, X.; Zhang, H.; Xie, F. Bottom-Up Nucleation Induced Conformal Crystallization for Inverted MA-Free Perovskite Solar Cells on Textured Substrates. *Chemical Engineering Journal* **2025**, *505*, No. 159390.
(28) Zheng, Y.; Tian, C.; Wu, X.; Sun, A.; Zhuang, R.; Tang, C.; Liu, Y.; Li, Z.; Ouyang, B.; Du, J.; Li, Z.; Wu, X.; Chen, J.; Cai, J.; Chen, C.-C. Dual-Interface Modification for Inverted Methylammonium-Free Perovskite Solar Cells of 25.35% Efficiency with Balanced Crystallization. *Adv. Energy Mater.* **2024**, *14* (20), No. 2304486.
(29) Wang, J.; Liu, N.; Liu, Z.; Liu, J.; Zhou, C.; Zhang, J.; Huang, L.; Hu, Z.; Zhu, Y.; Liu, X. Versatile Self-Assembled Monolayer Enables High-Performance Inverted $CsPbI_3$ Perovskite Solar Cells. *ACS Applied Nano Materials* **2024**, *7* (13), 15267−15276.
(30) Zhao, Y.; Luan, X.; Han, L.; Wang, Y. Post-Assembled Alkylphosphonic Acids for Efficient and Stable Inverted Perovskite Solar Cells. *Adv. Funct. Mater.* **2024**, *34* (46), No. 2405646.
(31) Li, X.; Ying, Z.; Zheng, J.; Wang, X.; Chen, Y.; Wu, M.; Xiao, C.; Sun, J.; Shou, C.; Yang, Z.; Zeng, Y.; Yang, X.; Ye, J. Surface Reconstruction for Efficient and Stable Monolithic Perovskite/Silicon Tandem Solar Cells with Greatly Suppressed Residual Strain. *Adv. Mater.* **2023**, *35* (30), No. 2211962.
(32) Gontkovskaya, V. T.; Kolpakov, V. A. Nonisothermal Processes in a System with Serial and Parallel Reactions under Conditions of Linear Heating. *Combustion, Explosion and Shock Waves* **1982**, *18* (3), 315−320.
(33) Valley, D. T.; Onstott, M.; Malyk, S.; Benderskii, A. V. Steric Hindrance of Photoswitching in Self-Assembled Monolayers of Azobenzene and Alkane Thiols. *Langmuir* **2013**, *29* (37), 11623−11631.
(34) Tan, Q.; Li, Z.; Luo, G.; Zhang, X.; Che, B.; Chen, G.; Gao, H.; He, D.; Ma, G.; Wang, J.; Xiu, J.; Yi, H.; Chen, T.; He, Z. Inverted Perovskite Solar Cells Using Dimethylacridine-Based Dopants. *Nature* **2023**, *620* (7974), 545−551.
(35) An, Q.; Fassl, P.; Hofstetter, Y. J.; Becker-Koch, D.; Bausch, A.; Hopkinson, P. E.; Vaynzof, Y. High Performance Planar Perovskite Solar Cells by ZnO Electron Transport Layer Engineering. *Nano Energy* **2017**, *39*, 400−408.
(36) Zhou, H.; Wang, W.; Duan, Y.; Sun, R.; Li, Y.; Xie, Z.; Xu, D.; Wu, M.; Wang, Y.; Li, H.; Fan, Q.; Peng, Y.; Yao, Y.; Liao, C.; Peng, Q.; Liu, S.; Liu, Z. Glycol Monomethyl Ether-Substituted Carbazolyl Hole-Transporting Material for Stable Inverted Perovskite Solar Cells with Efficiency of 25.52%. *Angew. Chem., Int. Ed.* **2024**, *63* (33), No. e202403068.
(37) Deng, J.; Huang, X.; Che, Y.; Wang, X.; Zhang, X.; Wu, B.; Yang, L.; Zhang, J. Salt-Based Catalyzer to Aid Heterogeneous Nucleation Enabling > 23% Efficient Electron-Transport-Layer-Free Perovskite Solar Cells. *Adv. Funct. Mater.* **2024**, *34*, No. 2408392.
(38) Yang, L.; Zhou, H.; Duan, Y.; Wu, M.; He, K.; Li, Y.; Xu, D.; Zou, H.; Yang, S.; Fang, Z.; Liu, S.; Liu, Z. 25.24%-Efficiency $FACsPbI_3$ Perovskite Solar Cells Enabled by Intermolecular Esterification Reaction of DL-Carnitine Hydrochloride. *Adv. Mater.* **2023**, *35* (16), No. 2211545.
(39) Liu, S.; Li, J.; Xiao, W.; Chen, R.; Sun, Z.; Zhang, Y.; Lei, X.; Hu, S.; Kober-Czerny, M.; Wang, J.; Ren, F.; Zhou, Q.; Raza, H.; Gao, Y.; Ji, Y.; Li, S.; Li, H.; Qiu, L.; Huang, W.; Zhao, Y.; Xu, B.; Liu, Z.; Snaith, H. J.; Park, N.-G.; Chen, W. Buried Interface Molecular Hybrid for Inverted Perovskite Solar Cells. *Nature* **2024**, *632* (8025), 536−542.
(40) Xiong, Z.; Chen, X.; Zhang, B.; Odunmbaku, G. O.; Ou, Z.; Guo, B.; Yang, K.; Kan, Z.; Lu, S.; Chen, S.; Ouedraogo, N. A. N.; Cho, Y.; Yang, C.; Chen, J.; Sun, K. Simultaneous Interfacial Modification and Crystallization Control by Biguanide Hydrochloride for Stable Perovskite Solar Cells with PCE of 24.4%. *Adv. Mater.* **2022**, *34* (8), No. 2106118.

https://doi.org/10.1021/acsami.4c22563
ACS Appl. Mater. Interfaces 2025, 17, 14269−14277

(41) Wang, S.; Khan, D.; Zhou, W.; Sui, Y.; Zhang, T.; Yu, G.; Huang, Y.; Yang, X.; Chen, X.; Yan, H.; Tang, J.; Yang, F.; Han, P.; Zheng, Z.; Zhang, Y.; Tang, Z. Ion-Dipole Interaction for Self-Assembled Monolayers: A New Strategy for Buried Interface in Inverted Perovskite Solar Cells. *Adv. Funct. Mater.* **2024**, *34* (27), No. 2316202.
(42) Wang, Y.; Wang, F.; Song, J.; Ye, J.; Cao, J.; Yin, X.; Su, Z.; Jin, Y.; Hu, L.; Zuilhof, H.; Li, Z.; Yan, W.; Gao, F. Ethyl Thioglycolate Assisted Multifunctional Surface Modulation for Efficient and Stable Inverted Perovskite Solar Cells. *Adv. Funct. Mater.* **2024**, *34* (38), No. 2402632.
(43) Cao, Q.; Wang, T.; Pu, X.; He, X.; Xiao, M.; Chen, H.; Zhuang, L.; Wei, Q.; Loi, H.-L.; Guo, P.; Kang, B.; Feng, G.; Zhuang, J.; Feng, G.; Li, X.; Yan, F. Co-Self-Assembled Monolayers Modified NiO*x* for Stable Inverted Perovskite Solar Cells. *Adv. Mater.* **2024**, *36* (16), No. 2311970.
(44) Deng, X.; Qi, F.; Li, F.; Wu, S.; Lin, F. R.; Zhang, Z.; Guan, Z.; Yang, Z.; Lee, C.-S.; Jen, A. K. Y. Co-Assembled Monolayers as Hole-Selective Contact for High-Performance Inverted Perovskite Solar Cells with Optimized Recombination Loss and Long-Term Stability. *Angew. Chem., Int. Ed.* **2022**, *61* (30), No. e202203088.
(45) Chalkias, D. A.; Nikolakopoulou, A.; Kontaxis, L. C.; Kalarakis, A. N.; Stathatos, E. Record-Breaking Efficient and Mechanically-Robust Ambient-Air-Processed Carbon-Based Flexible Perovskite Photovoltaics through Effective and Benign-to-Plastics Green-Antisolvent Quenching. *Adv. Funct. Mater.* **2024**, *34* (41), No. 2406354.
(46) Yang, L.; Zheng, F.; Wu, J.; Hou, Y.; Qi, X.; Miao, Y.; Wang, X.; Huang, L.; Liu, X.; Zhang, J.; Zhu, Y.; Hu, Z. Unveiling Local Current Behavior and Manipulating Grain Homogenization of Perovskite Films for Efficient Solar Cells. *ACS Nano* **2024**, *18* (27), 17547−17556.
(47) Ge, Z.; Qiao, J.; Song, J.; Li, X.; Fu, J.; Fu, Z.; Gao, J.; Tang, X.; Jiang, L.; Tang, Z.; Lu, G.; Hao, X.; Sun, Y. Suppressing Trap-Assisted Nonradiative Recombination via Interface Modification for Achieving Efficient Organic Solar Cells. *Adv. Energy Mater.* **2024**, *14* (22), No. 2400203.
(48) Yang, S.; Wu, M.; Lei, X.; Wang, J.; Han, Y.; He, X.; Liu, S.; Liu, Z. Ultra-High 1.27 V VOC of Pure $CsPbI_3$ Perovskite Solar Cells with an Efficiency of 21.8%. *ACS Energy Letters* **2024**, *9* (10), 4817−4826.

https://doi.org/10.1021/acsami.4c22563
ACS Appl. Mater. Interfaces 2025, 17, 14269−14277